

NGC 1261: An r -process enhanced globular cluster from the Gaia-Enceladus event [★]

Andreas J. Koch-Hansen¹, Camilla J. Hansen², and Andrew McWilliam³

¹ Zentrum für Astronomie der Universität Heidelberg, Astronomisches Rechen-Institut, Mönchhofstr. 12, 69120 Heidelberg, Germany

² Max-Planck Institut für Astronomie, Königstuhl 17, 69117 Heidelberg, Germany

³ Carnegie Observatories, 813 Santa Barbara St., Pasadena, CA 91101, USA

ABSTRACT

Our Milky Way (MW) has witnessed a series of major accretion events in the past. One of the later additions, the Gaia-Enceladus merger, has contributed a considerable mass to the inner Galaxy, but also generously donated to the outer halo. So far, associations with present-day MW globular clusters (GCs) have been chiefly based on their kinematics and ages. In this work, we present a chemical abundance study of the outer halo ($R_{GC} \sim 18$ kpc) GC NGC 1261, which has been suggested to be an accreted object based on its younger age. We measured 31 species of 29 elements in two stars from high-resolution Magellan/MIKE spectra and find that the cluster is moderately metal poor, at $[Fe/H] = -1.26$, with a low scatter of 0.02 dex. NGC 1261 is moderately α -enhanced to the 0.3 dex level. While from the small sample alone it is difficult to assert any abundance correlations, the light elements Na, O, Mg, and Al differ significantly between the two stars in contrast to the majority of other elements with smaller scatter; this argues in favor of multiple generations of stars coexisting in this GC. Intriguingly for its metallicity, NGC 1261 shows heavy element abundances that are consistent with r -process nucleosynthesis and we discuss their origin in various sites. In particular the Eu overabundance quantitatively suggests that one single r -process event, such as a neutron-star neutron-star merger or a rare kind of supernova, can be responsible for the stellar enhancement or even the enrichment of the cluster with the excess r material. Its heavy element pattern makes NGC 1261 resemble the moderately enhanced r -I stars that are commonly found in the halo and have been detected in Gaia-Enceladus as well. Therefore, combining all kinematical, age, and chemical evidence we conclude that NGC 1261 is a chemically intriguing GC that was born in the Gaia-Enceladus galaxy and has been subsequently accreted into the MW halo.

Key words. Stars: abundances – Galaxy: abundances – Galaxy: evolution – Galaxy: halo – globular clusters: individual: NGC 1261

1. Introduction

Globular clusters (GCs) play an important role in building up the Galactic halo and bulge during an intense period of tidal disruptions (Gnedin & Ostriker 1997; Odenkirchen et al. 2001; Martell & Grebel 2010; Schiavon et al. 2017; Koch et al. 2019a; Hanke et al. 2020b). Equal importance is given to the accretion of the GC system of the Milky Way (MW) per se, when merging dwarf galaxies get stripped of their GCs during their gradual disruption (e.g., Searle & Zinn 1978; Sarajedini & Layden 1995; Lee et al. 1999; Kruijssen et al. 2019; Malhan et al. 2019). Recently, several major merger events were identified in the action space that had opened up with the powerful Gaia satellite (Gaia Collaboration et al. 2018) and/or via chemical tagging. Amongst these are Gaia-Enceladus (Helmi et al. 2018; Belokurov et al. 2018), Sequoia (Myeong et al. 2019), and Heracles (Horta et al. 2021), all of which released stellar masses of a few $10^8 M_{\odot}$ (see also Naidu et al. 2021). As one of the later additions (8–11 Gyr ago), Gaia-Enceladus has contributed a considerable mass to the inner Galaxy, but also generously donated to the outer halo. In particular, Massari et al. (2019) infer that 28 of the Galactic GCs are dynamically related to Gaia-Enceladus. So far, associations of

such merger events with present-day MW GCs have been chiefly based on their kinematics and ages (Massari et al. 2019), while chemical tagging of both components is only available for a few cases (e.g., Koch & Côté 2019; Koch et al. 2019b; Horta et al. 2020).

In this work, we focus on the outer halo GC NGC 1261, which has been long suggested to be an accreted system based on a younger age of ~ 10.3 Gyr (Marín-Franch et al. 2009; Kravtsov et al. 2010). While the distance values reported in the literature range from 15.5 kpc to 17.2 kpc (Ferraro et al. 1999; Harris 1996; Baumgardt et al. 2019; Arellano Ferro et al. 2019), its location in the outer halo, at $R_{GC} \sim 18$ kpc, is undisputed. So far, chemical abundance information for this cluster is sparse, and, to our knowledge, the only previous study is that by Filler et al. (2012), who determined abundance ratios for 21 elements, but only reported on the GC mean and dispersion over their seven stars¹. The light elements, in particular Na and O, measured by Filler et al. (2012) show the strong variations that are commonly found across the Galactic GCs and that are strong indicators for the presence of multiple stellar populations in these systems (e.g., Cohen 1978; Carretta et al. 2009; Bastian & Lardo 2018).

In our present work, we further investigate the intrinsic properties of NGC 1261, but also attempt to place it in a Galactic framework by comparing our measured abundances to various

Send offprint requests to: A.J. Koch-Hansen; e-mail: andreas.koch@uni-heidelberg.de; hansen@mpia.de; andy@carnegiescience.edu

[★] This paper includes data gathered with the 6.5 meter Magellan Telescopes located at Las Campanas Observatory, Chile.

¹ Unfortunately, this work is only available as a AAS conference abstract and no details of the analysis are available.

in situ and ex situ MW components. A first step was taken by Filler et al. (2012), who suggested that this GC shows lower α -abundance ratios than otherwise found in systems at similar metallicity; our measurements, however, do not support these findings. It is interesting to note that Shipp et al. (2018) detected extratidal stars emanating stream-like from this GC, and an extended halo around NGC 1261 has been reported as well (Leon et al. 2000; Kuzma et al. 2018; Raso et al. 2020). In the complex web of stellar streams, Shipp et al. (2018) place particular emphasis on the EriPhe stellar overdensity (Li et al. 2016), which is suggested to be the remains of a tidally disrupted dwarf galaxy. Moreover, a potential original association of EriPhe with the Phoenix stream (Balbinot et al. 2016) and NGC 1261 is highlighted, prompting the need for detailed chemical tagging, as we embark on the present study.

This work is organized as follows: In Section 2 we introduce our target and observation strategies. Details on the chemical abundance analysis are given in Sect. 3, and the resulting abundance ratios are presented in Sect. 4. Next, Sect. 5 is dedicated to the r -process dominance in NGC 1261, before we discuss our findings in the context of an accretion origin from Gaia-Enceladus in Sect. 6.

2. Target selection, observations, and data reduction

Two stars were selected from the catalog of Kravtsov et al. (2010). Their choice was a trade off between avoiding the crowded, central regions of the GC, while opting for bright stars near the tip of the red giant branch (RGB). As a consequence of overall unfortunate weather conditions during the observing run, no more stars could be targeted. Our sample stars are shown in Fig. 1 together with the color-magnitude diagram (CMD) of Kravtsov et al. (2010) and an isochrone from the “a Bag of Stellar Tracks and Isochrones” (BASTI) grid (Hidalgo et al. 2018), matching the age, metallicity, distance, and reddening of NGC 1261.

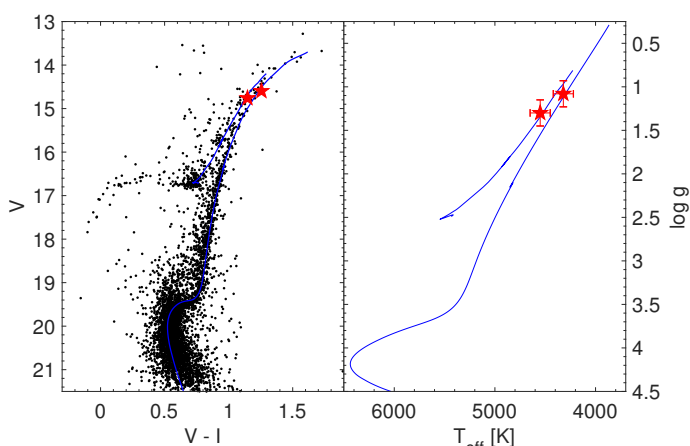


Fig. 1. CMD of NGC 1261 from the photometry of Kravtsov et al. (2010, left panel) and Kiel diagram (right panel). Our two targets are indicated as red symbols. Also shown is a 10.3 Gyr isochrone for the metallicity of our stars (Hidalgo et al. 2018).

Observations were carried out with the Magellan Inamori Kyocera Echelle (MIKE) spectrograph at the 6.5 m Magellan2/Clay Telescope at the Las Campanas Observatory, Chile during the night of Oct. 16, 2016. Under varying seeing conditions of ~ 1.3 – $2.2''$ we used a slit width of $0.5''$ and binned

the CCD pixels by 2×1 in spatial and spectral direction. This resulted in a resolving power of $R \sim 40,000$. We make use of the red and blue arms of the instrument, covering the wavelength range 3340 – 9150 \AA . The stars were exposed for 1 and 1.25 hours, which was split into four and three exposures, respectively, to facilitate cosmic ray removal.

The raw data were reduced within the pipeline of Kelson (2000; 2003) and subjected to flat field division, order tracing from quartz lamp flats, and a wavelength calibration from Th-Ar lamp exposures. As a result, the signal-to-noise ratios (S/N) of the spectra reach 30–40 per pixel near the peak on the order containing $H\alpha$, declining toward ~ 15 toward the blue at $\sim 4500 \text{ \AA}$. In Table 1 we list the basic observational, positional, and photometric properties of the target stars.

Radial velocities of the targets were determined by a cross-correlation of the red spectra against a synthetic spectrum of an RGB star with stellar parameters representative of our targets. This yielded typical uncertainties of $\sim 0.1 \text{ km s}^{-1}$. Clustering around a mean heliocentric value of $71.5 \pm 1.2 \text{ km s}^{-1}$, these stars are confirmed to be members with NGC 1261, which has been recently reported to have a systemic mean heliocentric velocity of $71.36 \pm 0.24 \text{ km s}^{-1}$ (Baumgardt et al. 2019). The small sample size of only two stars; however, inhibits an in-depth study of the dynamic properties of the GC.

3. Abundance analysis

The chemical composition of the two stars was determined from a standard analysis based on equivalent width (EW) measurements and spectral synthesis. For the former, we fitted Gaussian line profiles using the IRAF `splot` task. We built our analysis on the line list from Kacharov et al. (2013, and references therein) for the moderately metal-rich GC M 75. In order to obtain a fair balance of weak and strong lines, this was complemented with the Fe-line list of Ruchti et al. (2013), which was optimized for solar-metallicity stars. Further additions in the spectral synthesis in the blue or noisier spectral ranges are from Lawler et al. (2001, 2006, 2009), Den Hartog et al. (2003), and Hansen et al. (2013). Hyperfine splitting was included where appropriate (i.e., it was negligible for weaker lines) using data from Den Hartog et al. (2011), Hansen et al. (2013), Mashonkina & Christlieb (2014), Lawler et al. (2015, 2019), and Shi et al. (2018). In the actual abundance analysis we used the ATLAS grid of plane-parallel, 72-layer, one-dimensional, line-blanketed Kurucz models without convective overshoot. Moreover, the α -enhanced opacity distribution functions AODFNEW of (Castelli & Kurucz 2003) were adopted. We further adhered to local thermodynamic equilibrium (LTE) for all species. All computations employed the stellar abundance code MOOG (Snedden 1973, version 2014).

3.1. Stellar parameters

To first order, we estimated the effective temperatures based on the V and I photometry of Kravtsov et al. (2010) combined with the K magnitudes from 2MASS, and we adopted a reddening of 0.012 (Schlafly & Finkbeiner 2011). The metallicity to be adjusted in the calibrations of T_{eff} with V–I and V–K colors by Ramírez & Meléndez (2005) was initially set at the value reported by Harris (1996, 2010 version). The dispersion between results from the two color indices lies at 75 K on average.

Using those T_{eff} values, photometric gravities were computed. To this end, we adopted the latest distance to NGC 1261 of 15.5 kpc based on Gaia DR2 (Gaia Collaboration et al. 2018;

Table 1. Properties of the targeted stars.

ID ^a	α (J2000.0)	δ (J2000.0)	V [mag]	V-I [mag]	t_{exp} [s]	S/N ^b [pixel ⁻¹]	v_{HC} [km s ⁻¹]	T_{eff} [K]	log g [dex]	[Fe/H] [dex]	ξ [km s ⁻¹]
35	03:12:29.59	-55:11:30.19	14.597	1.256	4200	20/15/42/63	73.2	4320	1.08	-1.24	2.00
46	03:12:09.51	-55:14:58.051	14.760	1.147	3600	18/12/33/50	69.9	4550	1.30	-1.27	2.30

Notes. ^(a) Identifications from the catalog of Kravtsov et al. (2010). ^(b) Measured at 4500, 5200, 6600, and 8600 Å, which coincides with the peaks of the blaze function in the respective orders.

Baumgardt et al. 2019), but we note that the range of distances reported for this GC includes farther values out to 17.2 kpc (Arellano Ferro et al. 2019). Another source of uncertainty is the mass of the stars, which we took as 0.8 M_{\odot} . However, noting that star 46 may be on the asymptotic giant branch (AGB; see Fig. 1), a lower mass of $\sim 0.6 M_{\odot}$ is also feasible. Combined, all these error sources results in an overall uncertainty in the surface gravity of 0.15 dex.

In the next instance, the parameters were refined based on the balances of the iron abundance from neutral lines with excitation potential to settle T_{eff} , and with reduced width so as to fix the microturbulence ξ . The photometric and spectroscopic values are identical for star 35, while the latter is warmer by 110 K for star 46; we adopt the spectroscopic T_{eff} in the following. As an estimate for the $\sigma(T_{\text{eff}})$, we obtained the 1σ uncertainty in the slope of abundance versus excitation potential, combined with the sensitivity of the slope to T_{eff} . This results in an error on the spectroscopic temperature of 60 K.

Upon using the photometric gravities, ionization balance was not achieved for star 35, but the neutral and ionised iron species agreed to within 0.01 dex for star 46. This is addressed further in Sects. 4.1 and 4.3. We reiterate, however, the uncertainty in log g , which is able to resolve the imbalance (see also Sect. 3.2). At the metallicity of NGC 1261 of -1.26 dex, the GC stellar parameter study of Mucciarelli & Bonifacio (2020) indicates that spectroscopic parameters are still reliable and not affected by perturbations from, for example, departures from LTE. The final parameters for both stars are also contained in Table 1.

3.2. Abundance errors

For the statistical errors on our abundances we state in Table 2 with our abundance results the standard deviation and the number of lines measured per element to derive its abundance ratio. Secondly, we estimated systematic errors in the standard manner, that is, we varied each stellar parameter about its uncertainty as estimated in the previous section ($T_{\text{eff}} \pm 60$ K, log $g \pm 0.15$ dex, $[M/H] \pm 0.1$ dex, $\xi \pm 0.1$ km s⁻¹) and recorded the difference to the unperturbed parameter set. These deviations in log ϵ are listed in Table A.1 in the appendix for both stars. Furthermore, an identical analysis was performed, but with the solar-scaled opacity distributions (ODFNEW), where we take one-quarter of the respective deviation to reflect an uncertainty in the stars' $[\alpha/\text{Fe}]$ of 0.1 dex (listed as column "ODF" in Table A.1). Finally, we list the total systematic uncertainty as the squared sum of all contributions is given in the last column, although we caution that this is merely a conservative upper limit given the strong correlations between the various stellar parameters (e.g., McWilliam et al. 1995).

4. Abundance results

All resulting abundance ratios and the statistical error proxies are given in Table 2. In this work, we adopt the solar abundances of Asplund et al. (2009). In following Figures 2 through 5, we place these results into context with stars across the MW disks, bulge, and halo. References to the literature data are given in the captions.

Table 2. Abundance results.

Species	Star 35			Star 46			
	[X/Fe]	σ	N	[X/Fe]	σ	N	
Li I	<-1.60	...	1	<-0.50	...	1 ^S	S
O I	0.71	0.10	2	0.54	0.17	2	S
Na I	0.10	0.06	4	0.39	0.16	4	S
Mg I	0.34	0.20	9	0.49	0.18	6	
Al I	0.08	0.12	4	0.37	0.18	3	S
Si I	0.33	0.20	18	0.25	0.23	14	
K I	0.46	0.04	2	0.61	0.08	2	
Ca I	0.33	0.26	20	0.25	0.22	19	
Sc II	0.00	0.18	5	0.08	0.25	5	
Ti I	0.29	0.27	40	0.23	0.24	25	
Ti II	0.29	0.40	15	0.28	0.11	10	
V I	0.17	0.16	19	0.01	0.18	14	
Cr I	-0.06	0.21	13	-0.10	0.19	10	
Mn I	-0.35	0.15	6	-0.41	0.12	6	
Fe I	-1.24	0.21	162	-1.27	0.22	147	
Fe II	-1.15	0.17	16	-1.26	0.20	16	
Co I	0.03	0.20	4	-0.07	0.14	2	
Ni I	0.02	0.27	36	-0.04	0.26	28	
Cu I	-0.41	0.11	3	-0.31	0.15	2	
Zn I	-0.12	...	1	0.01	0.01	2	
Rb I	0.11	...	1	0.20	...	1	
Sr II	-0.20	...	1	>-0.70	...	1	
Y II	-0.08	0.34	5	0.08	0.28	5	S
Zr II	-0.27	...	1	0.13	...	1	S
Ba II	0.01	0.16	4	0.12	0.18	5	S
La II	0.27	0.11	4	0.36	0.07	3	S
Ce II	0.09	...	1	0.17	...	1	S
Nd II	0.25	...	1	0.33	...	1	S
Sm II	0.64	0.17	4	0.64	0.16	3	S
Eu II	0.60	0.21	2	0.58	0.21	2	S

Notes. "S" denotes abundances that were derived from spectrum synthesis. Ionized species and oxygen are referenced to ionized iron.

4.1. Iron abundance

From both stars, we find a mean metallicity of NGC 1261 of -1.26 ± 0.02 (stat.) ± 0.12 (sys.), which is in excellent agreement with the value listed in the Harris (1996) catalog. Other analyses, while differing at the 0.1 dex level, all agree that

this GC is only moderately metal poor: Kravtsov et al. (2010) finds $[\text{Fe}/\text{H}] = -1.34 \pm 0.16$ and -1.41 ± 0.10 dex, depending on the CMD features used, on the scale of Zinn & West (1984) using their wide-field U- and B-band photometry. In turn, the abundance analysis of seven stars from MIKE spectra by Filler et al. (2012) resulted in a similar value of -1.19 ± 0.02 dex, which is consistent with the scale of Kraft & Ivans (2003).

Ionization balance is marginally achieved for star 35 with $[\text{Fe I}/\text{II}] = -0.09 \pm 0.05$, while both Fe species agree very well in star 46, at $[\text{Fe I}/\text{II}] = -0.01 \pm 0.05$. To alleviate the discrepancy in the brighter star, a distance closer by 3 kpc or a much higher mass of $\sim 1.2 M_{\odot}$ would need to be imposed, neither of which are attractive options. While it is inconclusive from the CMD (Fig. 1), star 35 might also be on the AGB, in which case the surface gravity would decline, bringing the Fe abundances closer to ionization equilibrium. Lowering the helium mass fraction following Stromgren et al. (1982) and Lind et al. (2011) remains unphysical. As our error analysis shows, switching to the solar-scaled opacity distributions (ODFNEW) allows us to remove the ionization imbalance in star 35. However, this is not supported by the α -enhancements in the stars that are rather compatible with the enhanced opacity distributions. Finally, recomputing the iron abundances with a subset of those lines with available NLTE-corrections from Bergemann et al. (2012) only led to minor changes in $[\text{Fe}/\text{H}]$ from either species so that departures from LTE cannot impose the balance, neither. In the following, we continue with the bona fide parameter set, irrespective of the remaining ionization imbalance (see also the discussions in Koch & McWilliam 2008). Accordingly, abundance ratios of neutral species are always referenced against neutral Fe and those from ionized species against Fe II. Likewise, O I is referenced against Fe II since the two species are the dominant form and have similar gravity sensitivity.

4.2. Light elements: Li, C, O, Na, Al, K

Both lithium and carbon are barely detected in both stars; the limits we place on their abundance ratios are typical for luminous red giants in the field and in GCs (Lind et al. 2009; Placco et al. 2014; Kirby et al. 2015). We note, however, the presence of a Li-rich giant in this GC (Sanna et al. 2020).

As for oxygen, we note that its abundance was derived with explicit care of the underlying Ca-autoionization feature of the 6363 Å line and potential weak telluric absorption affecting either used line. The light elements O and Na are of great interest since their abundance ratio can be strongly affected by proton-burning reactions, a chemical signature of multiple GC subpopulations (e.g., Carretta et al. 2009). As shown in the left panel of Fig. 2 these elements also vary significantly in NGC 1261. While strongly enhanced in oxygen, the approximately solar value of $[\text{Na}/\text{Fe}]$ in star 46 can still be compatible with a second-generation star. Similarly, star 35 has both elevated Na and O levels.

Mg and Al abundances show large, correlated, dispersions in GC stars (e.g., Carretta et al. 2012), which is consistent with our results for NGC 1261 (right panel of Fig. 2). Unlike O and Na, however, the Al and Mg abundances are positively correlated. We simply conclude that the presence of abundance variations in NGC 1261, measured in this work, are in line with the finding of Filler et al. (2012) and we attribute the abundance differences to different GC subpopulations. Given the small size of our sample, we refrain from uniquely associating our stars with either first or second generation.

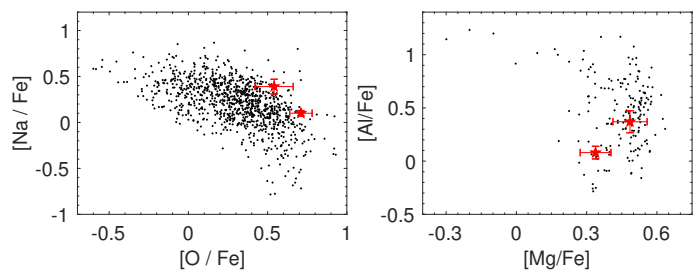


Fig. 2. Light element variations in NGC 1261 (red symbols) and the compilation of stars in 17 GCs from Carretta et al. (2009).

4.3. α -elements: Mg, Si, Ca, Ti

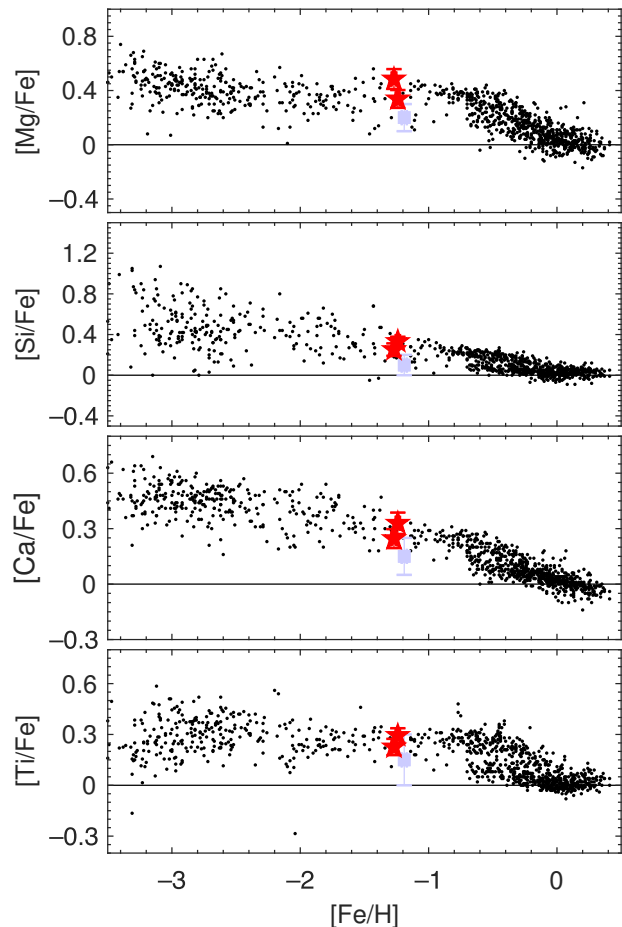


Fig. 3. Abundance results for the α -elements. Milky Way halo (Roediger et al. 2014) and disk (Bensby et al. 2014) stars are shown as black dots, and the mean values for NGC 1261 by Filler et al. (2012) are indicated in light blue.

The abundance ratios of the α -elements are shown in Fig. 3. We note that ionization equilibrium in Ti follows that of iron. While $\log \varepsilon(\text{Ti I}) - \log \varepsilon(\text{Ti II})$ takes values of -0.09 and -0.06 in stars 35 and 46, respectively, the abundance ratios relative to the respective species (viz. $[\text{Ti I}/\text{Fe I}]$ and $[\text{Ti II}/\text{Fe II}]$) are consistent to within the errors (see Table 2).

If we simplistically form a straight average of the four elements we measured, we find a mean $[\alpha/\text{Fe}]$ of 0.32 (star 35) and 0.30 dex (star 46). Overall, all elements show very low star-to-star scatter save for Mg, which we assign to the occurrence of multiple populations in this GC. These elevated values are in contrast to the numbers reported by Filler et al. (2012), who mea-

sured α /Fe ratios that are significantly lower than those found in halo stars of similar metallicity. Their study suggested values for [Mg,Si,Ca,Ti/Fe] of ~ 0.1 dex contrasting with the canonical halo plateau value of ~ 0.4 dex. Combined with the younger age of the cluster, the α -depletion with respect to systems at similar metallicities claimed by Filler et al. (2012) could suggest an accretion origin from a dwarf galaxy because those tend to have systematically lower $[\alpha/\text{Fe}]$ ratios, owing to their low star formation efficiencies (e.g., Matteucci & Brocato 1990; Koch et al. 2008; Tolstoy et al. 2009). We, however, revisit a possible accretion origin of NGC 1261 based on its actual α - and heavy element composition in Sects. 5 and 6.

4.4. Fe-peak elements: Sc, V, Cr, Mn, Co, Ni, Cu, Zn

Abundances for the eight (nine including Fe) iron-peak elements we were able to measure are shown in Figs. 4 and 5. There is

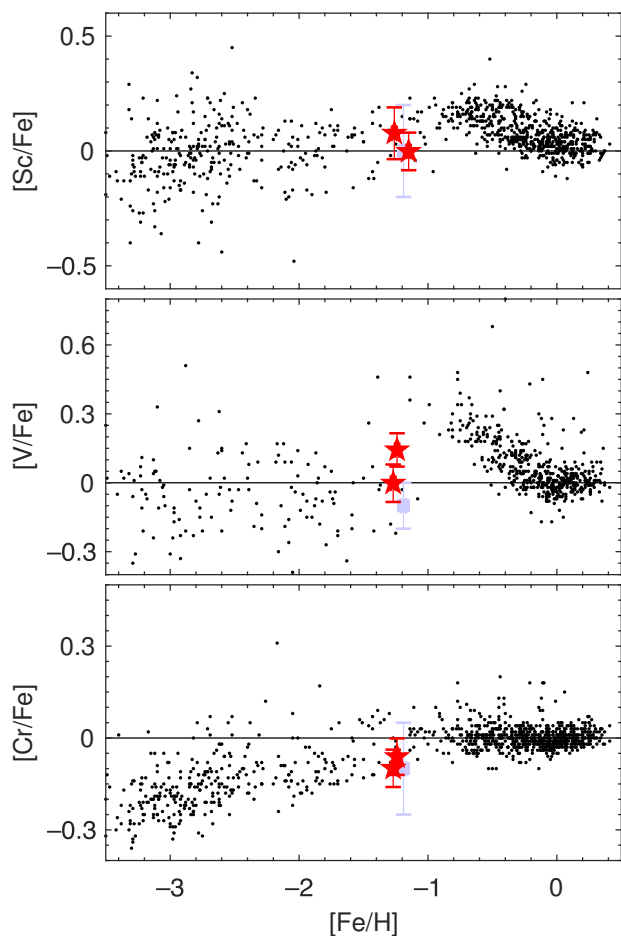


Fig. 4. Same as Fig. 3, but for Fe-peak elements. The values for Sc and V in the disk are from Battistini & Bensby (2015).

little to notice in the distribution of these elements and suffice it to say that they all follow the trends outlined by moderately metal-poor halo field stars, manifesting the origin of the Fe-peak in Supernovae (SNe) of type Ia. Both stars have similar abundance ratios and most values are also broadly consistent with the study of Filler et al. (2012).

5. *r*-process dominance

We were able to determine abundance ratios of the neutron-capture elements Rb, Sr, Y, Zr, Ba, La, Ce, Nd, Sm, and Eu.

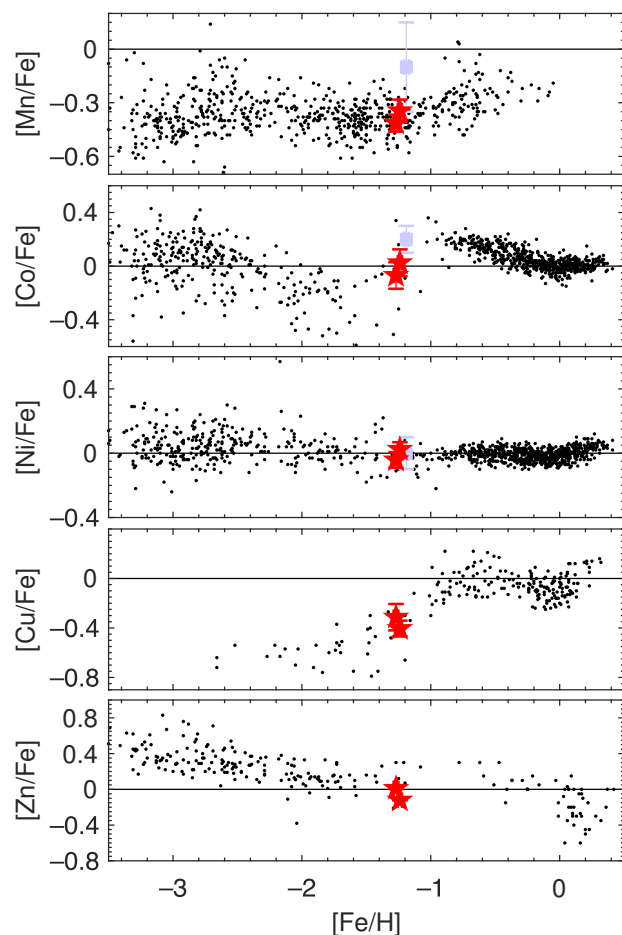


Fig. 5. Same as Fig. 3, but for the remaining Fe-peak elements. The data for Mn were taken from Sobeck et al. (2006), Co abundances from Battistini & Bensby (2015), and Cu in the MW halo and disks from the studies of Mishenina et al. (2002, 2011). The reference sample of Zn abundances in the MW is from Barbuy et al. (2015).

The values for Sr are rather to be taken as lower limits because of the strong saturation of the used 4215 Å line and the strong blending and uncertainty in the continuum placement owing to the low S/N ratio. We note, however, that the results from EW measurements and spectral synthesis agree. Ba abundances were determined from the 4554, 5853, 6141, 6496 Å lines, while our [Eu/Fe] is based on the red lines at 6437 and 6645 Å.

A subset of the heavy element abundances are shown in Fig. 6. While Zn, Y, and Ba are consistent with the approximately solar values as seen in the halo field, we note a slight enhancement in [La/Fe] at the 0.3-dex level. Most strikingly, however, the [Eu/Fe] ratio is very high – at 0.6 dex. This is bolstered by the work of Filler et al. (2012), who report an even larger overabundance 0.7 dex from their seven stars. We note that our values have not been corrected for NLTE. Mashonkina & Christlieb (2014) estimate Eu-corrections on the order of 0.1 dex, albeit for a more metal-poor sample, which would result in even larger [Eu/Fe] ratios in our stars.

In order to further investigate the origin of the heavy elements in NGC 1261, we juxtapose in Fig. 7 the solar-scaled *s*- and *r*-process contributions (Burris et al. 2000). The overlap of the cluster stars and the *r*-process track is striking, and the full heavy-element abundance pattern can best be reproduced (in a least-squares sense) by an almost pure *r*-pattern with a 5–10% admixture of *s*-process yields. The *r*-process dominance of

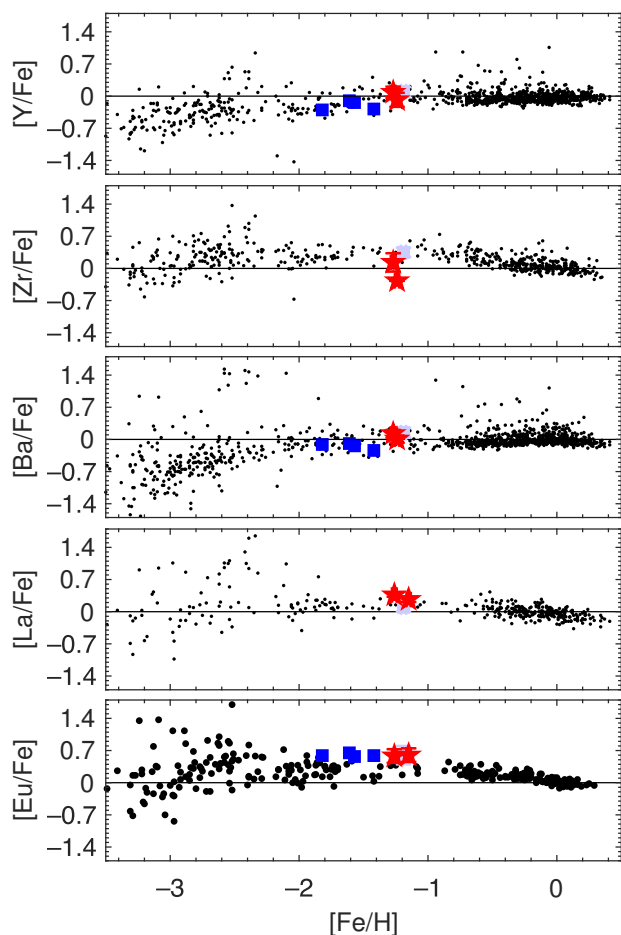


Fig. 6. Same as Fig. 3, but for the neutron-capture elements ($Z > 30$). Zr and La abundances of disk stars are from Battistini & Bensby (2016). Here, all axes are on the same scale so as to facilitate comparing the enhancements. The r -rich stars associated with Gaia Enceladus are shown as blue squares (Aguado et al. 2021).

NGC 1261 is further highlighted when comparing its patterns to metal-poor halo field star CS22892–052 (Sneden et al. 2003), which is governed by r -process nucleosynthesis.

The $[\text{Ba}/\text{Fe}]$ and $[\text{Eu}/\text{Fe}]$ ratios of the stars qualify them as r -I stars², although those are primarily found at lower metallicities (Westin et al. 2000; Beers & Christlieb 2005)³. Comparing our NGC 1261 stars to two well-known r -II (CS 22895-052) and r -I (HD20; Hanke et al. 2020a) stars, a clear r -process trend lying between these two r -I and r -II stars is seen despite the higher metallicity of stars 35 and 46. Surprisingly, even the lighter ($37 \leq Z < 50$) elements seem to follow a smooth r -process trends.

5.1. Lighter n -capture elements (Rb, Sr, Y, Zr)

The lighter n -capture elements (Rb, Sr, Y, and Zr) can be produced in weak s - and r -processes as well as their main channels. The Rb abundance can be used as a tracer of the n -density or n -exposure in the n -capture environments (e.g., Pignatari et al. 2010). Classically speaking, Sr, Y, and Zr are predominantly

² Such r -I stars are classified via $0.3 \leq [\text{Eu}/\text{Fe}] \leq 1.0$ and $[\text{Ba}/\text{Eu}] < 0$. Similarly, the strongly enhanced r -II stars are defined via $[\text{Eu}/\text{Fe}] > 1.0$ and $[\text{Ba}/\text{Eu}] < 0$ (Beers & Christlieb 2005).

³ We also note the existence of r -I stars at moderately low metallicity in the Galactic bulge (Johnson et al. 2013).

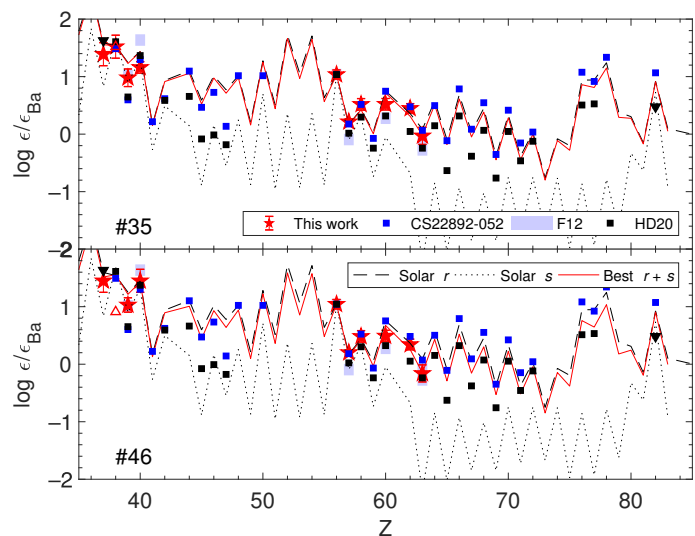


Fig. 7. Heavy element distributions of both target stars. Also shown are the solar-scaled curves from Burris et al. (2000) and the r -rich benchmark stars CS22892–052 and HD20 (Sneden et al. 2003; Hanke et al. 2020a). The mean and standard deviations of the NGC 1261 sample of Filler et al. (2012, “F12”) are indicated as blue shaded boxes. All patterns are normalized to Barium.

formed in the s -process in the solar inventory. However, the large star-to-star scatter detected in these elements (e.g., François et al. 2007; Hansen et al. 2012) indicate that several processes may contribute to their production at the metal-poor end of the metallicity scale (see also McWilliam 1998). Studies have shown that a lighter element primary process (LEPP; see, e.g., Busso et al. 1999; Travaglio et al. 2004; Bisterzo et al. 2012; Hansen et al. 2014), including the alpha-rich freeze-out (Woosley & Hoffman 1992), can contribute to their production, while other yield computations may be able to explain a larger contribution through model effects such as rotation in AGB stars (e.g., Piersanti et al. 2013; Cristallo et al. 2015a). The weak s -process is typically associated with fast-rotating massive stars (FRMS; Hirschi 2007; Frischknecht et al. 2016; Choplin et al. 2018). The fast rotation in combination with C- reactions leads to the n -excess that facilitates a weak s -process, which, relatively speaking, produces more Sr, Y, Zr than Ba and La. Hence, the ratio of Y/La may be used to trace weak versus main s -process contributions, but it may also be attributed to the mass and metallicity of the AGB donor (Busso et al. 1999). Recently, Sr was shown in the direct observations of kilonova AT2017gfo to be produced in the merger of two neutron stars (Watson et al. 2019). Hence, as most n -capture processes need to pass the $A \sim 90$ region, a complex mixture of contributions from various processes can be expected in the formation of Rb-Zr. Finally, the Galactic GC M15 ($[\text{Fe}/\text{H}] \sim -2.4$) is included in our comparison that follows owing to its heavy (r -process) element content, where traces of a scatter in the light n -capture elements, and even more so in the heavy elements, have been found (Sneden et al. 1997; Otsuki et al. 2006; Worley et al. 2013). This indicates contributions from several processes forming light and heavy elements in differing amounts, or it calls for incomplete mixing.

5.2. Source of the Eu overabundance

Despite the variance between the light element abundances, the similarity of the $[\text{Eu}/\text{Fe}]$ ratios in our two stars is consistent with the possibility that the r -process enhancement in NGC 1261 is

primordial. Clearly, chemical analysis of many more than two stars in the cluster is required to test this idea.

If the *r*-process enhancement is of primordial origin, then the excess mass of Eu in the cluster can be estimated from the enhancement of the NGC 1261 [Eu/Fe] ratio, at +0.6 dex, which is approximately 0.3 dex higher than typical MW stars with similar [Fe/H], combined with the expected total initial mass of stars in NGC 1261, at $1.32 \times 10^6 M_{\odot}$ (Webb & Leigh 2015). In this way, we find an excess europium mass of $2 \times 10^{-5} M_{\odot}$, assuming that the total star formation efficiency of the primordial molecular cloud was close to unity. This europium mass is close to the predicted ejected *r*-process masses, at 3×10^{-5} and $5 \times 10^{-5} M_{\odot}$, for two individual neutron star-neutron star (NS) merger cases studied by Goriely et al. (2011). If we adopt the europium *r*-process mass fraction of 0.01, implicit in Goriely et al. (2011), we estimate a total *r*-process mass for NGC 1261 of $2 \times 10^{-3} M_{\odot}$, which is similar to a predicted total mass of *r*-process ejecta for NS merger scenarios in the range 10^{-3} to $10^{-2} M_{\odot}$ (e.g., Goriely et al. 2011; Shibata & Hotokezaka 2019, and references therein).

If the total star formation efficiency of the NGC 1261 parent molecular cloud was not close to unity, then the measured *r*-process abundances might be explained by multiple NS merger events or an upward revision of the predicted *r*-process yields (e.g., Molero et al. 2021). We note that the predicted mass of ejected *r*-process material for NS mergers is sensitive to the equation of state of the NS, the mass ratio of the binary, and whether the merger is with another NS or a black hole (e.g., Shibata & Hotokezaka 2019).

We finally note that magneto-rotational SNe could also be a possible site of the *r*-process material, in which case the higher α -abundance could be easily explained. However, as seen in Reichert et al. (2021a,b) there might not be a direct link between the α - and *r*-process enhancement and in such SNe the *r*-process Eu production might be a bit lower ($\sim 5 \times 10^{-6} M_{\odot}$).

5.3. Comparison with *s*- and *r*-rich globular clusters

5.3.1. Origin of the heavy elements

Figure 8 shows selected heavy element ratios (Zn/Rb, Zr/Rb, Y/La, and Eu/La)⁴ from which we can gain insight into the heavy element enrichment of stars 35 and 46. For comparison, we selected clusters of similar metallicity with well-populated chemical abundance patterns and with clear *r*- and *s*-process dominance. In this case, M4 and M5 (Yong et al. 2008a,b) have a matching [Fe/H] of ~ -1.2 dex and a stronger *s*- and *r*-process contribution, respectively. Another GC with a scaled *r*-process pattern is the slightly more metal-poor NGC 6752 ([Fe/H] ~ -1.6), where the elements between Ba and Dy are seen to follow a solar-scaled, *r*-process distribution (Yong et al. 2005).

The [Ba/Eu] ratio is oft-used to provide information on the relative *s/r* ratio in the stars (e.g., Spite 1992; Hansen et al. 2018). The high values of [Eu/Ba] and [Eu/La] strongly indicate that the stars in NGC 1261 are *r*-process dominated (see Fig. 8), where the “pure” limits are placed according to *s*- ([Eu/La]_{*s*} ~ -1.0) and *r*-fractions ([Eu/La]_{*r*} ~ 0.4), computed following Arlandini et al. (1999). In turn, the observed low [Zn/Rb] and [Zr/Rb] ratios could indicate a high neutron density or exposure leading to a slight relative overabundance of Rb (at [Rb/Fe] ~ 0.15 dex). To this effect, we also illustrate the trends of varying respective model parameters in Fig. 8. The weak-*s*

⁴ We note that we explicitly chose to avoid Fe in any of these figures because it clouds the *r*- and *s*-process traces we seek (see, e.g., Hansen et al. 2012).

computations in Pignatari et al. (2010) indicate that increasing *n*-exposure and -density ultimately increase the Rb and other *s*-process element abundances. In particular, using solar abundances and the production factors from their Table 9 shows that [Zn/Rb] reaches from just subsolar to ~ -0.3 dex with increasing *n*-density and -exposure. The exact value depends on the model employed.

In particular, [Zr/Rb] suggests a contribution from more massive AGB stars (Yong et al. 2006, 2008a) in NGC 1261, as we also verified by comparison with the AGB yields of the FR.U.I.T.Y. database (Cristallo et al. 2011, 2015b). A $1.3 M_{\odot}$ AGB model with $Z=0.001$ and no rotation yields a [Zr/Rb] ratio of ~ 0.4 dex, while a more massive ($5 M_{\odot}$) AGB with the same Z yields a much lower value (~ -0.4 dex). The high [Y/La] seen in M4 clearly confirms its stronger *s*-process contribution, while the low ratios in NGC 1261, M5, and M15 indicate a relatively low *s*-process contribution, which may originate from the weak *s* or, alternatively, from metal-poor AGB stars of higher mass. A strong main *s*-process contribution would be expected for a $2 M_{\odot}$ AGB star (with the same Z as given above), leading to [Y/La] ~ -0.6 . Overall, the AGB mass is generally the dominant *s*-process nucleosynthesis governor, while metallicity is normally a mere secondary parameter as shown in, for example, Hansen et al. (2018, their Figs. 12, 13).

Typical light *s*-to-heavy *s* ratios in FRMS would, via the weak *s*-process, produce values greater than zero as is predicted for [Sr/Ba] > 0 (see, e.g., Frischknecht et al. 2012). This is in excellent agreement with the high [Eu/La] detected in NGC 1261, which is only rivaled by the more metal-poor M15. A slight *s*-process contribution is expected at the moderately high [Fe/H] ~ -1.2 of NGC 1261, and it is therefore not surprising that M15 would show a cleaner and stronger *r*-process imprint. Finally, we note that the intermediate neutron capture process (*i*-process; Cowan & Rose 1977) is unlikely as the source of the heavy elements in NGC 1261 because that would lead to higher positive [Ba/La] ratios (Hempel et al. 2016; Reichert et al. 2021a), while our measured value is negative.

5.3.2. Heavy-element spreads

Various elements and their line-to-line standard deviation are shown in Fig. 9. The top panel shows element abundances normalized to Eu (*r*-process), the middle panel shows abundances scaled to Rb (weak *s*), and the bottom panel shows the 1σ star-to-star scatter. When scaling to the *r*-process element Eu, a large scatter is seen between the lighter-to-heavy element ratios as is also common in metal-poor field stars (Roederer et al. 2018; Hansen et al. 2012). However, strong differences also occur between the more *s*-rich M4 and the other *r*-process dominated clusters. The largest difference with respect to Eu is seen for Sr, where Sr in NGC 1261 is only a lower limit, thereby decreasing this spread likely to the level of the Y/Eu variation if a detection on Sr could be placed in NGC 1261.

The [element/Rb] ratio tracing a lighter element (likely in a weak *s*-process) appears to show less of a spread amongst the GCs. We note, however, that fewer clusters have Rb detections, so this comparison may not be fair or complete. The lighter elements O and Na are known for their intra-cluster spreads, which is related to the occurrence of multiple populations in the GCs. However, the bottom panel of Fig. 9 indicates that larger scatters are also seen in some heavier elements. For several elements and in several clusters, a large variation is detected, notably for Zr in NGC 1261, but also in the heavy elements like Eu. The latter is mainly driven by M15, which is known to have a high degree of

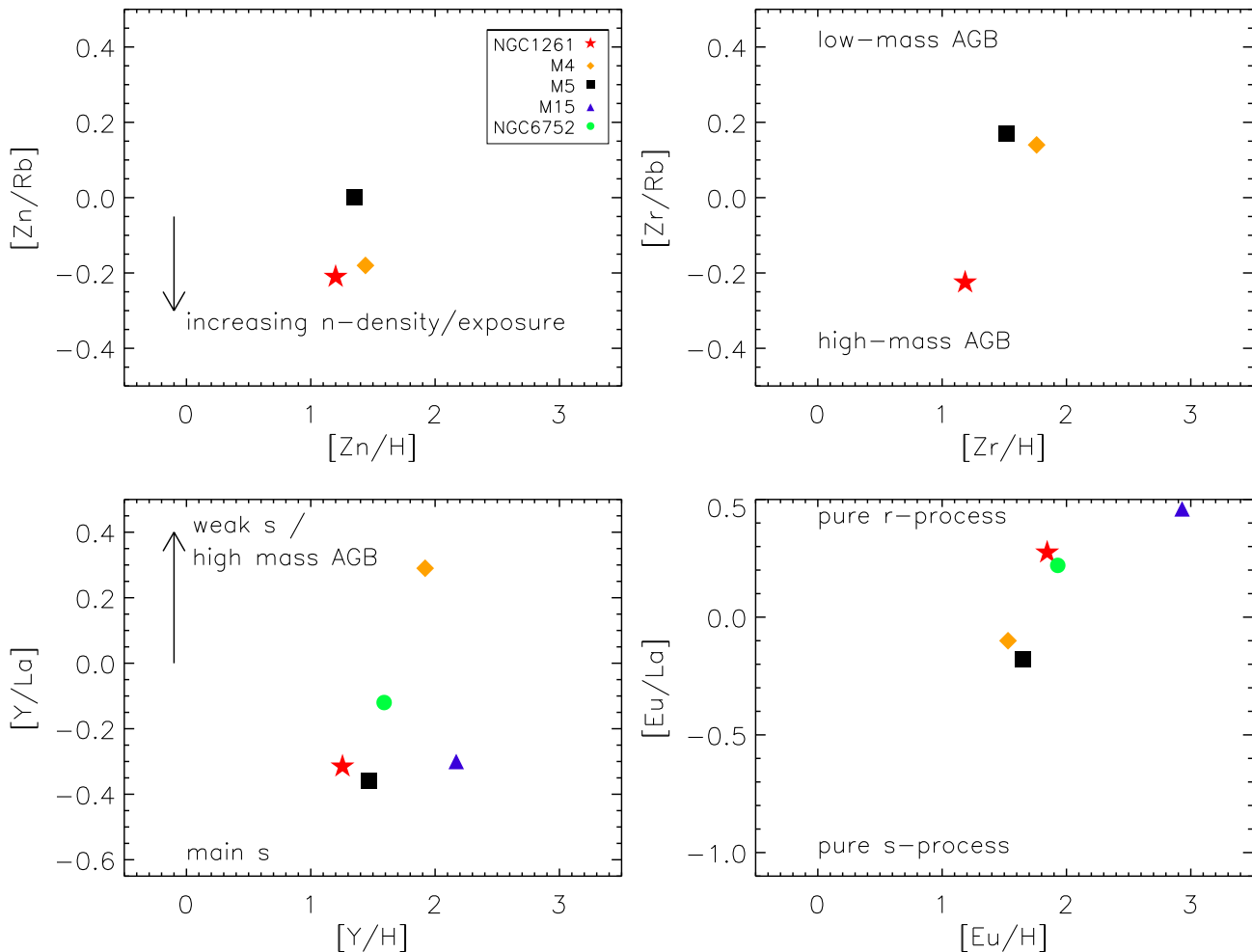


Fig. 8. Abundance ratios for selected elements that are tracers of the origins of the n -capture elements in NGC 1261 and reference GCs. Shown are the average values of the respective stellar samples. The illustrative trends and nucleosynthetic distinctions in each panel are based on computations from Pignatari et al. (2010, Zn/Rb), Cristallo et al. (2015b, Zr/Rb), Frischknecht et al. (2012, Y/La), and Arlandini et al. (1999, Eu/La). See main text for discussions.

heavy n -capture spread (Snedden et al. 1997; Otsuki et al. 2006; Worley et al. 2013). Finally, a high Zr abundance and spread could also be produced if a weak r -process were also active in NGC 1261, as discussed in Hansen et al. (2012), and may as such not point directly toward the mass of the AGB. In particular, the numerous processes that contribute to the region around $A \sim 90$ complicate tracing their production at such relatively high metallicities.

6. Discussion and conclusions: The origin of NGC 1261

Based on ages and orbital properties, Massari et al. (2019) associated NGC 1261 with the Gaia-Enceladus merger event (Helmi et al. 2018; Belokurov et al. 2018), which not only built a major fraction of the Galactic inner and outer halos (e.g., Naidu et al. 2021) but must also have lost parts of its GC system to the outer halo (e.g., Kruijssen et al. 2019). An accretion origin of this GC is in line with its younger age (Marín-Franch et al. 2009; Kravtsov et al. 2010). In particular, Massari et al. (2019) asserted that all but one of the 28 GCs dynamically associated with Gaia-Enceladus have apocenters closer than 25 kpc, which

also holds true for NGC 1261, where Baumgardt et al. (2019) found a close pericenter of 1.4 kpc and an apocenter distance of 20 kpc.

Thus far, the merger-GC ties are likely, but to further sculpt this picture, the addition of a chemical abundance space is imperative (e.g., Nissen & Schuster 1997, 2010). In Fig. 10, we overplot the mean $\langle [\alpha/Fe] \rangle$ ratio, defined as the straight average of the Mg, Si, Ca, and Ti abundances⁵, for NGC 1261, a sample of reference GCs that are a potential Gaia-Enceladus prodigy, and the stellar content of Gaia-Enceladus itself (as contours).

Overall, NGC 1261 appears chemically very similar to Gaia-Enceladus in that it occupies the same mean metallicity and α -enhancement, irrespective of the large abundance spread in the massive parent galaxy. Monty et al. (2020) report on the α -elements in Gaia-Enceladus and fit a toy model to their distribution with metallicity; in this work, the location of the knee, that is, the downturn in $[\alpha/Fe]$ upon the onset of Fe-producing SNe Ia, lies at ~ -1.7 dex, placing it into the regime of the massive Galactic satellite Fornax (Hendricks et al. 2014; Reichert et al.

⁵ If we exclude Ti from the average as a result of its partial production in processes other than α -captures (e.g., Kobayashi et al. 2006), the mean α -enhancement increases merely by 0.02 dex.

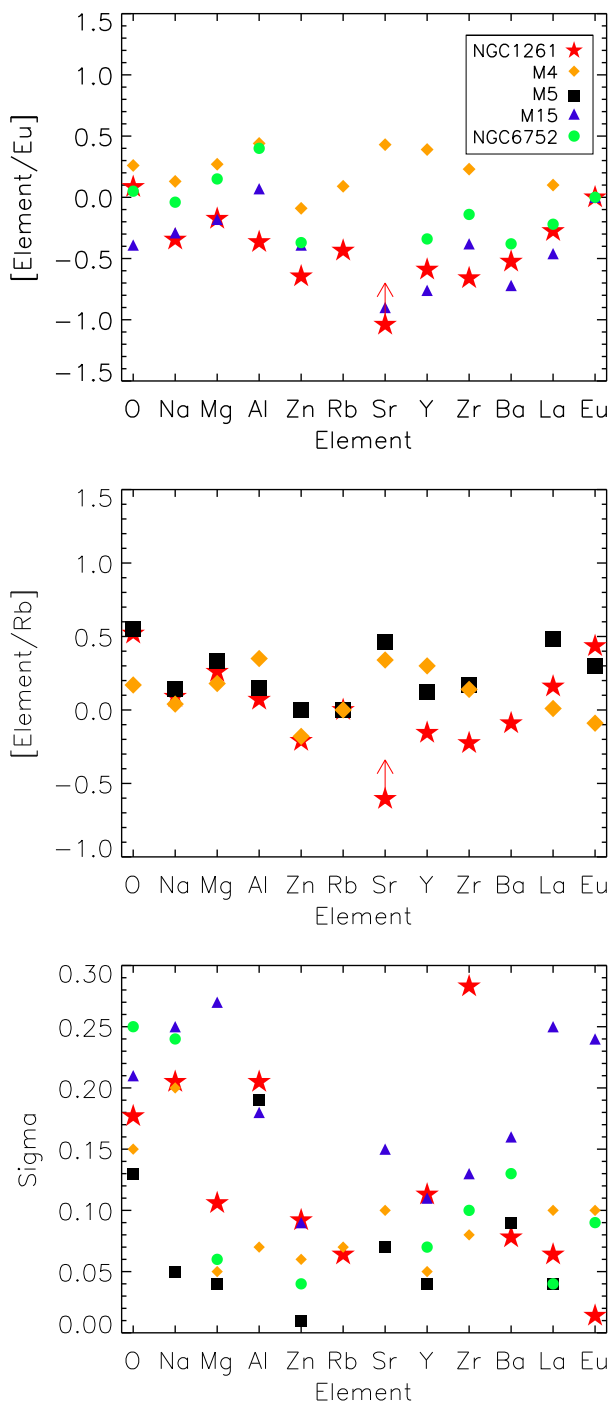


Fig. 9. Selected element ratios relative to Eu (top panel) and Rb (middle) for NGC 1261 and the reference GCs. The bottom panel indicates the 1σ star-to-scatter in each GC.

2020). Accordingly, Gaia-Enceladus stars at the same metallicity as NGC 1261 are expected to exhibit an $[a/Fe]$ ratio of ~ 0.3 dex, which fully agrees with our measured values.

The most important information can be gleaned from the heavy neutron-capture elements. Moderately *r*-process enriched r-I and r-II stars in the Galactic halo are often found to have chemodynamic associations amongst each other, arguing for an origin in common, disrupted objects (e.g., Roederer et al. 2018; Gudín et al. 2021), although the fraction of bona fide accreted

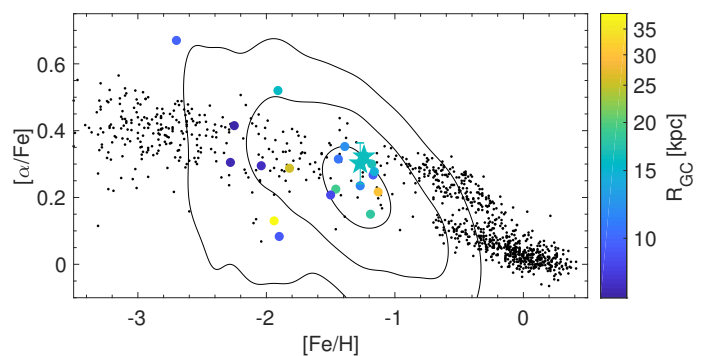


Fig. 10. Averaged $\langle [Mg, Si, Ca, Ti/Fe] \rangle$ ratio for MW stars (black dots) and NGC 1261 (star symbols). The stellar component of Gaia-Enceladus (Helmi et al. 2018) is overlaid as 1, 2, and 3σ contours. A sample of reference GCs dynamically associated with Gaia-Enceladus, color-coded by their Galactocentric distance, are shown. The GC abundances from the literature are from Francois (1991), McWilliam et al. (1992), Shetrone & Keane (2000), Cohen & Melendez (2005), Carretta et al. (2011), Roederer & Sneden (2011), Kacharov et al. (2013), Lovisi et al. (2013), Khamidullina et al. (2014), Koch & McWilliam (2014), Yong et al. (2014), Roederer & Thompson (2015), Carretta et al. (2013), Johnson et al. (2017), Marino et al. (2017), and Koch et al. (2019b).

stars is not fully known due to the limited sample sizes. While similar enrichment mechanisms are likely to happen in the halo field the large fraction and preponderance of *r*-rich stars in faint dwarf galaxies is striking (e.g., Ji et al. 2016; Hansen et al. 2018; Reichert et al. 2021a). Gaia-Enceladus also stands out in that it shows strong enhancement in the neutron-capture elements (Aguado et al. 2021; Matsuno et al. 2021). In particular, the $[Eu/Fe]$ ratios for the four stars in Aguado et al. (2021, see Fig. 7) are compatible with our findings in NGC 1261, albeit at slightly lower metallicities of -2.1 to -1.4 dex, placing them in the border region of r-I and r-II stars. By comparison with kinematically selected Gaia-Enceladus stars from the Galah survey (Buder et al. 2021), Aguado et al. (2021) highlight that the over-enhancements of $0.3 < [Eu/Fe] < 1$ seen over the entire metallicity range of the progenitor (sampled over ~ 1 dex) is a clear sign of *r*-process nucleosynthesis dominating the chemical evolution of this accreted satellite. This is clearly also seen in the associated NGC 1261, where similar enrichment took place before the GC was, still partly intact, accreted onto the MW.

Exploring further a possible dwarf galaxy connection, we compare stars 35 and 46 to the recently discovered Eu-rich stars in Fornax (Reichert et al. 2021a). These three stars have $-1.3 < [Fe/H] < -0.8$ hence making for a reasonable small comparison sample in a more massive satellite. The absolute Eu abundance of the three Eu stars in Fornax amount to almost 1 dex, which compares to a $\log \varepsilon(Eu)$ in NGC 1261 close to -0.1 dex. Hence, the formation mechanism and/or mixing in Fornax and NGC 1261 must differ, despite the very similar $[Fe/H]$ of the samples, and we expect both different formation mechanisms and mixing scenarios to be at work. Given the similarity of the $[Eu/Fe]$ ratios in the two stars analyzed in this work, we may consider that the Eu enrichment is primordial and did not occur after the stars formed. However, if the GC was enriched after one, or more, generations of stars formed, then stars below the turn-off must have even larger *r*-process abundances. At the turn-off magnitude of $V \sim 19.5$ mag, such a study is currently observationally too challenging to probe in statistically meaningful numbers.

Returning to the question of whether NGC 1261 could be associated with either the EriPhe overdensity or the Phoenix stel-

lar stream, as advocated by Shipp et al. (2018), the need for detailed chemical tagging of halo substructures is undisputed (e.g., Ji et al. 2020; Hansen et al. 2020; Naidu et al. 2020; Prudil et al. 2021). In this context we note that Ji et al. (2020) find that their sample of eight Phoenix stream stars are very metal poor, at <-2.6 dex, and thus lie far below the metallicity we reported for our target cluster. Unless the Phoenix progenitor had a large mass allowing for an abundance spread of more than 1.5 dex (cf. Koch 2009; Kirby et al. 2013), we do not support any association with NGC 1261.

Acknowledgements. We thank the anonymous referee for a positive and constructive report and are grateful to Moritz Reichert for helpful discussions. AJKH gratefully acknowledges funding by the Deutsche Forschungsgemeinschaft (DFG, German Research Foundation) – Project-ID 138713538 – SFB 881 (“The Milky Way System”), subprojects A03, A05, A11. This project was developed in part at the Streams 21 meeting, virtually hosted by the Flatiron Institute.

References

- Aguado, D. S., Belokurov, V., Myeong, G. C., et al. 2021, *ApJ*, 908, L8
- Arellano Ferro, A., Bustos Fierro, I. H., Calderón, J. H., & Ahumada, J. A. 2019, *Rev. Mexicana Astron. Astrofis.*, 55, 337
- Arlandini, C., Käppeler, F., Wisshak, K., et al. 1999, *ApJ*, 525, 886
- Asplund, M., Grevesse, N., Sauval, A. J., & Scott, P. 2009, *ARA&A*, 47, 481
- Balbinot, E., Yanny, B., Li, T. S., et al. 2016, *ApJ*, 820, 58
- Barbuy, B., Friaça, A. C. S., da Silveira, C. R., et al. 2015, *A&A*, 580, A40
- Bastian, N. & Lardo, C. 2018, *ARA&A*, 56, 83
- Battistini, C. & Bensby, T. 2015, *A&A*, 577, A9
- Battistini, C. & Bensby, T. 2016, *A&A*, 586, A49
- Baumgardt, H., Hilker, M., Sollima, A., & Bellini, A. 2019, *MNRAS*, 482, 5138
- Beers, T. C. & Christlieb, N. 2005, *ARA&A*, 43, 531
- Belokurov, V., Erkal, D., Evans, N. W., Koposov, S. E., & Deason, A. J. 2018, *MNRAS*, 478, 611
- Bensby, T., Feltzing, S., & Oey, M. S. 2014, *A&A*, 562, A71
- Bergemann, M., Hansen, C. J., Bautista, M., & Ruchti, G. 2012, *A&A*, 546, A90
- Bisterzo, S., Gallino, R., Straniero, O., Cristallo, S., & Käppeler, F. 2012, *MNRAS*, 422, 849
- Buder, S., Sharma, S., Kos, J., et al. 2021, *MNRAS*
- Burris, D. L., Pilachowski, C. A., Armand roff, T. E., et al. 2000, *ApJ*, 544, 302
- Busso, M., Gallino, R., & Wasserburg, G. J. 1999, *ARA&A*, 37, 239
- Carretta, E., Bragaglia, A., Gratton, R., & Lucatello, S. 2009, *A&A*, 505, 139
- Carretta, E., Lucatello, S., Gratton, R. G., Bragaglia, A., & D’Orazi, V. 2011, *A&A*, 533, A69
- Carretta, E., D’Orazi, V., Gratton, R. G., & Lucatello, S. 2012, *A&A*, 543, A117
- Carretta, E., Bragaglia, A., Gratton, R. G., et al. 2013, *A&A*, 557, A138
- Castelli, F. & Kurucz, R. L. 2003, in *IAU Symposium*, Vol. 210, *Modelling of Stellar Atmospheres*, ed. N. Piskunov, W. W. Weiss, & D. F. Gray, A20
- Choplan, A., Hirschi, R., Meynet, G., et al. 2018, *A&A*, 618, A133
- Cohen, J. G. 1978, *ApJ*, 223, 487
- Cohen, J. G. & Melendez, J. 2005, *AJ*, 129, 1607
- Cowan, J. J. & Rose, W. K. 1977, *ApJ*, 212, 149
- Cristallo, S., Piersanti, L., Straniero, O., et al. 2011, *ApJS*, 197, 17
- Cristallo, S., Abia, C., Straniero, O., & Piersanti, L. 2015a, *ApJ*, 801, 53
- Cristallo, S., Straniero, O., Piersanti, L., & Gobrecht, D. 2015b, *ApJS*, 219, 40
- Den Hartog, E. A., Lawler, J. E., Sneden, C., & Cowan, J. J. 2003, *ApJS*, 148, 543
- Den Hartog, E. A., Lawler, J. E., Sobeck, J. S., Sneden, C., & Cowan, J. J. 2011, *ApJS*, 194, 35
- Ferraro, F. R., Messineo, M., Fusi Pecci, F., et al. 1999, *AJ*, 118, 1738
- Filler, D., Ivans, I. I., & Simmerer, J. 2012, in *American Astronomical Society Meeting Abstracts*, Vol. 219, *American Astronomical Society Meeting Abstracts #219*, 152.05
- François, P., Depagne, E., Hill, V., et al. 2007, *A&A*, 476, 935
- François, P. 1991, *A&A*, 247, 56
- Frischknecht, U., Hirschi, R., & Thielemann, F.-K. 2012, *A&A*, 538, L2
- Frischknecht, U., Hirschi, R., Pignatari, M., et al. 2016, *MNRAS*, 456, 1803
- Gaia Collaboration, Brown, A. G. A., Vallenari, A., et al. 2018, *A&A*, 616, A1
- Gnedin, O. Y. & Ostriker, J. P. 1997, *ApJ*, 474, 223
- Goriely, S., Bauswein, A., & Janka, H.-T. 2011, *ApJ*, 738, L32
- Gudin, D., Shank, D., Beers, T. C., et al. 2021, *ApJ*, 908, 79
- Hampel, M., Stancliffe, R. J., Lugaro, M., & Meyer, B. S. 2016, *ApJ*, 831, 171
- Hanke, M., Hansen, C. J., Ludwig, H.-G., et al. 2020a, *A&A*, 635, A104
- Hanke, M., Koch, A., Prudil, Z., Grebel, E. K., & Bastian, U. 2020b, *A&A*, 637, A98
- Hansen, C. J., Primas, F., Hartman, H., et al. 2012, *A&A*, 545, A31
- Hansen, C. J., Bergemann, M., Cescutti, G., et al. 2013, *A&A*, 551, A57
- Hansen, C. J., Montes, F., & Arcones, A. 2014, *ApJ*, 797, 123
- Hansen, C. J., El-Souri, M., Monaco, L., et al. 2018, *ApJ*, 855, 83
- Hansen, T. T., Riley, A. H., Strigari, L. E., et al. 2020, *ApJ*, 901, 23
- Harris, W. E. 1996, *AJ*, 112, 1487
- Helmi, A., Babusiaux, C., Koppelman, H. H., et al. 2018, *Nature*, 563, 85
- Hendricks, B., Koch, A., Lanfranchi, G. A., et al. 2014, *ApJ*, 785, 102
- Hidalgo, S. L., Pietrinferni, A., Cassisi, S., et al. 2018, *ApJ*, 856, 125
- Hirschi, R. 2007, *A&A*, 461, 571
- Horta, D., Schiavon, R. P., Mackereth, J. T., et al. 2020, *MNRAS*, 493, 3363
- Horta, D., Schiavon, R. P., Mackereth, J. T., et al. 2021, *MNRAS*, 500, 1385
- Ji, A. P., Frebel, A., Simon, J. D., & Chiti, A. 2016, *ApJ*, 830, 93
- Ji, A. P., Li, T. S., Hansen, T. T., et al. 2020, *AJ*, 160, 181
- Johnson, C. I., Rich, R. M., Kobayashi, C., et al. 2013, *ApJ*, 765, 157
- Johnson, C. I., Caldwell, N., Rich, R. M., & Walker, M. G. 2017, *AJ*, 154, 155
- Kacharov, N., Koch, A., & McWilliam, A. 2013, *A&A*, 554, A81
- Khamidullina, D. A., Sharina, M. E., Shimansky, V. V., & Davoust, E. 2014, *Astrophysical Bulletin*, 69, 409
- Kirby, E. N., Cohen, J. G., Guhathakurta, P., et al. 2013, *ApJ*, 779, 102
- Kirby, E. N., Guo, M., Zhang, A. J., et al. 2015, *ApJ*, 801, 125
- Kobayashi, C., Umeda, H., Nomoto, K., Tominaga, N., & Ohkubo, T. 2006, *ApJ*, 653, 1145
- Koch, A. 2009, *Astronomische Nachrichten*, 330, 675
- Koch, A. & McWilliam, A. 2008, *AJ*, 135, 1551
- Koch, A., Grebel, E. K., Gilmore, G. F., et al. 2008, *AJ*, 135, 1580
- Koch, A. & McWilliam, A. 2014, *A&A*, 565, A23
- Koch, A. & Côté, P. 2019, *A&A*, 632, A55
- Koch, A., Grebel, E. K., & Martell, S. L. 2019a, *A&A*, 625, A75
- Koch, A., Xi, S., & Rich, R. 2019b, *A&A*, 627, A70
- Kraft, R. P. & Ivans, I. I. 2003, *PASP*, 115, 143
- Kravtsov, V., Alcaño, G., Marconi, G., & Alvarado, F. 2010, *A&A*, 516, A23
- Kruijssen, J. M. D., Pfeffer, J. L., Reina-Campos, M., Crain, R. A., & Bastian, N. 2019, *MNRAS*, 486, 3180
- Kuzma, P. B., Da Costa, G. S., & Mackey, A. D. 2018, *MNRAS*, 473, 2881
- Lawler, J. E., Den Hartog, E. A., Sneden, C., & Cowan, J. J. 2006, *ApJS*, 162, 227
- Lawler, J. E., Sneden, C., Cowan, J. J., Ivans, I. I., & Den Hartog, E. A. 2009, *ApJS*, 182, 51
- Lawler, J. E., Sneden, C., & Cowan, J. J. 2015, *ApJS*, 220, 13
- Lawler, J. E., Hala, Sneden, C., et al. 2019, *ApJS*, 241, 21
- Lawler, J. E., Wickliffe, M. E., den Hartog, E. A., & Sneden, C. 2001, *ApJ*, 563, 1075
- Lee, Y. W., Joo, J. M., Sohn, Y. J., et al. 1999, *Nature*, 402, 55
- Leon, S., Meylan, G., & Combes, F. 2000, *A&A*, 359, 907
- Li, T. S., Balbinot, E., Mondrik, N., et al. 2016, *ApJ*, 817, 135
- Lind, K., Primas, F., Charbonnel, C., Grundahl, F., & Asplund, M. 2009, *A&A*, 503, 545
- Lind, K., Charbonnel, C., Decressin, T., et al. 2011, *A&A*, 527, A148
- Lovisi, L., Mucciarelli, A., Lanzoni, B., et al. 2013, *ApJ*, 772, 148
- Malhan, K., Ibata, R. A., Carlberg, R. G., Valluri, M., & Freese, K. 2019, *ApJ*, 881, 106
- Marín-Franch, A., Aparicio, A., Piotto, G., et al. 2009, *ApJ*, 694, 1498
- Marino, A. F., Milone, A. P., Yong, D., et al. 2017, *ApJ*, 843, 66
- Martell, S. L. & Grebel, E. K. 2010, *A&A*, 519, A14
- Mashonkina, L. & Christlieb, N. 2014, *A&A*, 565, A123
- Massari, D., Koppelman, H. H., & Helmi, A. 2019, *A&A*, 630, L4
- Matsuno, T., Hirai, Y., Tarumi, Y., et al. 2021, *A&A*, 650, A110
- Matteucci, F. & Brocato, E. 1990, *ApJ*, 365, 539
- McWilliam, A., Geisler, D., & Rich, R. M. 1992, *PASP*, 104, 1193
- McWilliam, A., Preston, G. W., Sneden, C., & Searle, L. 1995, *AJ*, 109, 2757
- McWilliam, A. 1998, *AJ*, 115, 1640
- Mishenina, T. V., Kovtyukh, V. V., Soubiran, C., Travaglio, C., & Busso, M. 2002, *A&A*, 396, 189
- Mishenina, T. V., Gorbaneva, T. I., Basak, N. Y., Soubiran, C., & Kovtyukh, V. V. 2011, *Astronomy Reports*, 55, 689
- Molero, M., Simonetti, P., Matteucci, F., & della Valle, M. 2021, *MNRAS*, 500, 1071
- Monty, S., Venn, K. A., Lane, J. M. M., Lokhorst, D., & Yong, D. 2020, *MNRAS*, 497, 1236
- Mucciarelli, A. & Bonifacio, P. 2020, *A&A*, 640, A87
- Myeong, G. C., Vasiliev, E., Iorio, G., Evans, N. W., & Belokurov, V. 2019, *MNRAS*, 1731
- Naidu, R. P., Conroy, C., Bonaca, A., et al. 2020, *ApJ*, 901, 48
- Naidu, R. P., Conroy, C., Bonaca, A., et al. 2021, *arXiv e-prints*, arXiv:2103.03251
- Nissen, P. E. & Schuster, W. J. 1997, *A&A*, 326, 751
- Nissen, P. E. & Schuster, W. J. 2010, *A&A*, 511, L10
- Odenkirchen, M., Grebel, E. K., Rockosi, C. M., et al. 2001, *ApJ*, 548, L165
- Otsuki, K., Honda, S., Aoki, W., Kajino, T., & Mathews, G. J. 2006, *ApJ*, 641, L117

- Piersanti, L., Cristallo, S., & Straniero, O. 2013, *ApJ*, 774, 98
- Pignatari, M., Gallino, R., Heil, M., et al. 2010, *ApJ*, 710, 1557
- Placco, V. M., Frebel, A., Beers, T. C., & Stancliffe, R. J. 2014, *ApJ*, 797, 21
- Prudil, Z., Hanke, M., Lemasle, B., et al. 2021, *A&A*, 648, A78
- Ramírez, I. & Meléndez, J. 2005, *ApJ*, 626, 465
- Raso, S., Libralato, M., Bellini, A., et al. 2020, *ApJ*, 895, 15
- Reichert, M., Hansen, C. J., Hanke, M., et al. 2020, *A&A*, 641, A127
- Reichert, M., Hansen, C. J., & Arcones, A. 2021a, *ApJ*, 912, 157
- Reichert, M., Obergaulinger, M., Eichler, M., Aloy, M. A., & Arcones, A. 2021b, *MNRAS*, 501, 5733
- Roederer, I. U. & Sneden, C. 2011, *AJ*, 142, 22
- Roederer, I. U., Preston, G. W., Thompson, I. B., et al. 2014, *AJ*, 147, 136
- Roederer, I. U. & Thompson, I. B. 2015, *MNRAS*, 449, 3889
- Roederer, I. U., Hattori, K., & Valluri, M. 2018, *AJ*, 156, 179
- Ruchti, G. R., Bergemann, M., Serenelli, A., Casagrande, L., & Lind, K. 2013, *MNRAS*, 429, 126
- Sanna, N., Franciosini, E., Pancino, E., et al. 2020, *A&A*, 639, L2
- Sarajedini, A. & Layden, A. C. 1995, *AJ*, 109, 1086
- Schiavon, R. P., Zamora, O., Carrera, R., et al. 2017, *MNRAS*, 465, 501
- Schlafly, E. F. & Finkbeiner, D. P. 2011, *ApJ*, 737, 103
- Searle, L. & Zinn, R. 1978, *ApJ*, 225, 357
- Shetrone, M. D. & Keane, M. J. 2000, *AJ*, 119, 840
- Shi, J. R., Yan, H. L., Zhou, Z. M., & Zhao, G. 2018, *ApJ*, 862, 71
- Shibata, M. & Hotokezaka, K. 2019, *Annual Review of Nuclear and Particle Science*, 69, 41
- Shipp, N., Drlica-Wagner, A., Balbinot, E., et al. 2018, *ApJ*, 862, 114
- Sneden, C. A. 1973, PhD thesis, The University of Texas at Austin.
- Sneden, C., Kraft, R. P., Shetrone, M. D., et al. 1997, *AJ*, 114, 1964
- Sneden, C., Cowan, J. J., Lawler, J. E., et al. 2003, *ApJ*, 591, 936
- Sobeck, J. S., Ivans, I. I., Simmerer, J. A., et al. 2006, *AJ*, 131, 2949
- Spite, M. 1992, in *The Stellar Populations of Galaxies*, ed. B. Barbuy & A. Renzini, Vol. 149, 123
- Stromgren, B., Gustafsson, B., & Olsen, E. H. 1982, *PASP*, 94, 5
- Tolstoy, E., Hill, V., & Tosi, M. 2009, *ARA&A*, 47, 371
- Travaglio, C., Gallino, R., Arnone, E., et al. 2004, *ApJ*, 601, 864
- Watson, D., Hansen, C. J., Selsing, J., et al. 2019, *Nature*, 574, 497
- Webb, J. J. & Leigh, N. W. C. 2015, *MNRAS*, 453, 3278
- Westin, J., Sneden, C., Gustafsson, B., & Cowan, J. J. 2000, *ApJ*, 530, 783
- Woosley, S. E. & Hoffman, R. D. 1992, *ApJ*, 395, 202
- Worley, C. C., Hill, V., Sobeck, J., & Carretta, E. 2013, *A&A*, 553, A47
- Yong, D., Grundahl, F., Nissen, P. E., Jensen, H. R., & Lambert, D. L. 2005, *A&A*, 438, 875
- Yong, D., Aoki, W., Lambert, D. L., & Paulson, D. B. 2006, *ApJ*, 639, 918
- Yong, D., Karakas, A. I., Lambert, D. L., Chieffi, A., & Limongi, M. 2008a, *ApJ*, 689, 1031
- Yong, D., Lambert, D. L., Paulson, D. B., & Carney, B. W. 2008b, *ApJ*, 673, 854
- Yong, D., Roederer, I. U., Grundahl, F., et al. 2014, *MNRAS*, 441, 3396
- Zinn, R. & West, M. J. 1984, *ApJS*, 55, 45

Appendix A: Systematic errors

Table A.1. Systematic error analysis.

Species	T_{eff} ± 60 K	$\log g$ ± 0.15 dex	[M/H] ± 0.1 dex	ξ ± 0.1 km s $^{-1}$	ODF	Sys.
O I	± 0.01	± 0.07	± 0.04	∓ 0.01	-0.12	0.09
	± 0.01	± 0.06	± 0.04	∓ 0.02	-0.11	0.08
Na I	± 0.05	∓ 0.01	∓ 0.01	∓ 0.03	+0.02	0.06
	± 0.05	∓ 0.01	∓ 0.01	∓ 0.04	+0.02	0.07
Mg I	± 0.04	∓ 0.01	± 0.00	∓ 0.06	-0.02	0.07
	± 0.05	∓ 0.01	∓ 0.00	∓ 0.07	-0.00	0.09
Al I	± 0.04	∓ 0.00	∓ 0.00	∓ 0.01	+0.01	0.04
	± 0.05	∓ 0.00	∓ 0.01	∓ 0.01	+0.02	0.05
Si I	∓ 0.03	± 0.04	± 0.02	∓ 0.02	-0.05	0.06
	∓ 0.01	± 0.02	± 0.01	∓ 0.02	-0.03	0.03
K I	± 0.11	∓ 0.00	∓ 0.01	∓ 0.12	-0.06	0.16
	± 0.09	∓ 0.00	∓ 0.02	∓ 0.12	-0.02	0.15
Ca I	± 0.07	∓ 0.01	∓ 0.01	∓ 0.10	-0.00	0.12
	± 0.07	∓ 0.01	∓ 0.01	∓ 0.08	+0.02	0.11
Sc II	∓ 0.01	± 0.07	± 0.03	∓ 0.08	-0.11	0.11
	∓ 0.01	± 0.06	± 0.03	∓ 0.07	-0.10	0.10
Ti I	± 0.11	∓ 0.01	∓ 0.01	∓ 0.09	-0.01	0.14
	± 0.11	∓ 0.00	∓ 0.02	∓ 0.06	+0.02	0.13
Ti II	∓ 0.02	± 0.06	± 0.03	∓ 0.10	-0.10	0.12
	∓ 0.01	± 0.05	± 0.03	∓ 0.10	-0.09	0.12
V I	± 0.12	∓ 0.00	∓ 0.01	∓ 0.04	-0.01	0.13
	± 0.11	∓ 0.00	∓ 0.01	∓ 0.02	+0.02	0.11
Cr I	± 0.10	∓ 0.01	∓ 0.01	∓ 0.09	-0.00	0.14
	± 0.10	∓ 0.01	∓ 0.02	∓ 0.08	+0.02	0.13
Mn I	± 0.10	∓ 0.00	∓ 0.01	∓ 0.05	+0.01	0.11
	± 0.09	± 0.01	∓ 0.00	∓ 0.14	-0.02	0.17
Fe I	± 0.04	± 0.01	± 0.00	∓ 0.08	-0.03	0.09
	± 0.06	± 0.00	∓ 0.00	∓ 0.07	+0.00	0.09
Fe II	∓ 0.12	± 0.07	± 0.04	∓ 0.06	-0.12	0.16
	∓ 0.05	± 0.06	± 0.03	∓ 0.05	-0.10	0.10
Co I	± 0.05	± 0.02	± 0.01	∓ 0.04	-0.03	0.07
	± 0.07	± 0.01	∓ 0.00	∓ 0.02	+0.00	0.07
Ni I	± 0.03	± 0.03	± 0.01	∓ 0.06	-0.05	0.08
	± 0.05	± 0.01	± 0.00	∓ 0.05	-0.01	0.07
Cu I	± 0.05	± 0.02	± 0.01	∓ 0.01	-0.03	0.07
	± 0.07	± 0.02	∓ 0.01	∓ 0.01	-0.01	0.07
Zn I	∓ 0.04	± 0.05	± 0.02	∓ 0.08	-0.07	0.11
	∓ 0.02	± 0.03	± 0.02	∓ 0.06	-0.06	0.07
Rb I	± 0.07	∓ 0.01	∓ 0.01	∓ 0.01	0.01	0.07
	± 0.07	∓ 0.01	∓ 0.01	∓ 0.01	0.02	0.07
Sr II	± 0.02	± 0.02	± 0.04	∓ 0.01	-0.10	0.06
	± 0.02	± 0.03	± 0.04	∓ 0.05	-0.11	0.08
Y II	∓ 0.01	± 0.06	± 0.03	∓ 0.11	-0.10	0.13
	∓ 0.01	± 0.06	± 0.03	∓ 0.06	-0.10	0.09
Zr II	± 0.01	± 0.05	± 0.02	∓ 0.12	-0.07	0.13
	± 0.01	± 0.05	± 0.02	∓ 0.07	-0.08	0.09
Ba II	± 0.02	± 0.06	± 0.03	∓ 0.14	-0.12	0.16
	± 0.02	± 0.05	± 0.04	∓ 0.12	-0.10	0.14
La II	± 0.01	± 0.07	± 0.04	∓ 0.01	-0.11	0.09
	± 0.01	± 0.06	± 0.04	∓ 0.01	-0.11	0.08
Ce II	± 0.01	± 0.06	± 0.03	∓ 0.02	-0.10	0.08
	± 0.01	± 0.06	± 0.03	∓ 0.01	-0.09	0.07
Nd II	± 0.01	± 0.06	± 0.03	∓ 0.05	-0.10	0.09
	± 0.01	± 0.06	± 0.03	∓ 0.04	-0.10	0.08
Sm II	± 0.02	± 0.06	± 0.03	∓ 0.05	-0.10	0.09
	± 0.02	± 0.06	± 0.03	∓ 0.04	-0.09	0.08
Eu II	∓ 0.01	± 0.07	± 0.04	∓ 0.03	-0.12	0.09
	∓ 0.01	± 0.06	± 0.03	∓ 0.01	-0.10	0.07

Notes. For each element, the respective top row refers to star 35, while the second one each is for star 46.